Supplementary Information

Materials and Methods

Diblock copolymer OS30 (PEO_{56}-$PS_{28,}$ M_n 5.5 kg/mol), OS90 (PEO_{193}-$PS_{86,}$ M_n 17.5 kg/mol), AB2 (PAA_{75}-$PBD_{103,}$ M_n 11.05 kg/mol), and OB18 (PEO_{80}-PBD_{125}, M_n 10.4 kg/mol) were from Polymersource Inc. OB9 (PEO_{50}-PBD_{54}, M_n 5.2 kg/mol) was from the Bates group at the University of Minnesota. Mw/Mn of the polymers ranged from 1.05 to 1.1. Chloroform, Xylene, Toluene, glass slides and cover slips were from Fisher. The hydrophobic dye PKH26 was from Sigma-Aldrich. The HCC-100A temperature controller from Dagan Corp. was used to control the temperature on a peltier heat stage to study the temperature dependent stiffness of the worms. FRAP measurements were performed using the VSL-337 laser-dye excitation arrangement (Coumarin dye) from LSI Laser Science Inc. Franklin, MA. AFM imaging was done on a Bioscope II atomic force microscope from Digital Instruments, Santa Barbara, CA.

Preparation of Worm Micelles. Worm micelles were prepared by the co-solvent evaporation method. Briefly, 10-50 μL of copolymer stock solution was put into a clean glass vial, and the chloroform evaporated under nitrogen. A controlled amount of chloroform is added back along with 1 ml of water to fluidize the core and enable worm formation. After 6-12 hours of hydration in the closed vial, leaving the vial open at 4 ^oC overnight evaporates out the chloroform, leaving a purely aqueous micelle solution. For the solvent fluidization experiments, given amount of chloroform, xylene or toluene was added back to the dry film, and retained in the solution and worm core by keeping the vial closed at all times.

Fluorescence Microscopy and FRAP. The cores of the micelles were labeled by 1 μL hydrophobic fluorophore PKH26 to enable visualization under fluorescence microscopy. The

experimental chamber was prepared by placing 5-10 μL of the worm solution between a glass slide and a 2.5 x 2.5 cm cover slip. Photobleaching of the worms was performed in two ways: In the first method, an aperture in the light path was used to selectively bleach the PKH26 dye in a section of the worm, and recovery monitored by opening the aperture fully. In the second method, a focused laser beam passed along the same light path as the fluorescent lamp was used to quickly overexpose a very small portion of the worm, resulting in more precise and rapid measurements.

Engineering worm shape in shear flow. Worm micelles were formed under stirring in an attempt to create shear induced straightening during the hydration process. The worms were formed in 15 x 45 mm amber vials, stirred by a 1.5 x 8 mm flea stir bar from Fischer Scientific. A Corning PC-420 stir plate was used at settings 4 and 7, which correspond to speeds of 155 and 550 RPM respectively according to the manufacturer.

Simulation Details and Methodology

Due to the large system size and longer time scales involved in these PEO-PS worms, coarse-grained (CG) based molecular dynamics simulation (CG-MD) is the ideal methodology to study the self-assembly of di-block co-polymers like PEO-PS. CG models have been routinely used to study self-assembly of different biological, as well as synthetic soft materials, including polymers, peptides, proteins, and membranes in science and engineering[1-6]. Within this paper we utilize long-time CG-MD to characterize structural and dynamical properties of single PEO-PS worm-like micelles composed of diblock copolymers of similar lengths that have been studied experimentally. The CG parameters for PS we use here are developed by Drenscko and Loverde[7]. They adopt a Shinoda-DeVane-Klein (SDK) [8] coarse-graining approach to model PS. The parameters for PEO and water are developed by the Klein group[5, 9, 10]. Intra-molecular interactions in the SDK model are calculated via harmonic potentials given by $V_{bond}(r) = K_b(r - r_0)^2$ and

$V_{angle}(\theta) = K_a(\theta - \theta_0)^2$, respectively. Here, K_b and r_0 are the equilibrium force constant and distance for bond stretch, and K_a and θ_0 are the equilibrium bending force constant and equilibrium value for angles. Non-bonded interactions are set by a pair-wise additive potential based on the Lennard-Jones (LJ) potential: $U_{LJ9-6} = (27/4)\varepsilon\{(\sigma/r)^9 - (\sigma/r)^6\}$ or $U_{LJ12-4} = (3\sqrt{3}/2)\varepsilon\{(\sigma/r)^{12} - (\sigma/r)^4\}$ [11]. Interactions between the PEO and PS are estimated assuming a combination rule between the PEG-CG bead, *i*, and PS CG group, *j*, where $\varepsilon_{ij} = (\varepsilon_{ii}\varepsilon_{jj})^{1/2}$ and $\sigma_{ij} = (\sigma_{ii} + \sigma_{jj})/2$. We also characterize the effect of hydrophobic solvent in the hydrophobic core of the PS, using a model hydrophobic bead to mimic the fluidizing effect of solvent on the micelle morphology. The solvent LJ parameters, both ε and σ, are the same as a single bead of the PS chain.

Worm micelle hinges For the purpose of this paper, a hinge is defined as a point along the worm

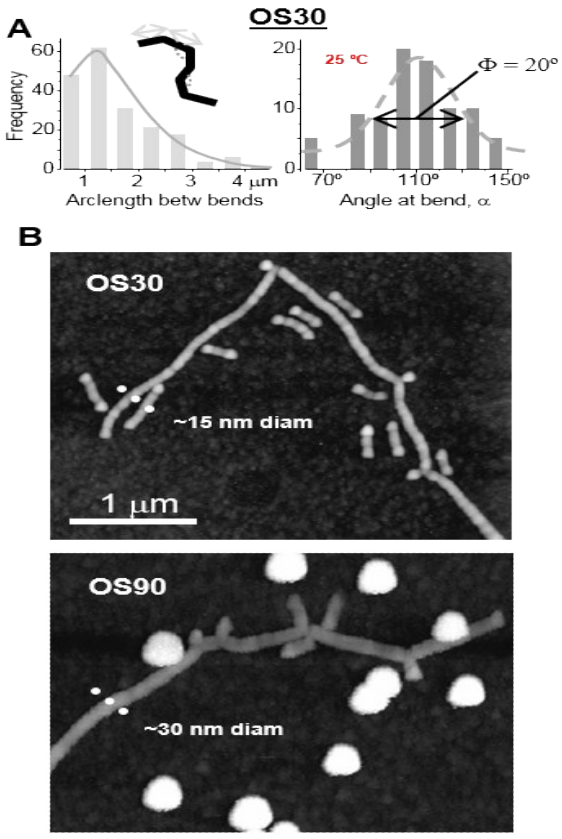

SI-1. Distance and angles between hinges in OS30 worms. (A). The worm backbones were digitized as 0.5 micron segments and deviations greater than 30 degree angle between neighboring segments were counted as bends. The distance between bends has a peak at ~ 1-1.5 microns, while the angles have a slightly more uniform distribution with a slight peak around 110-120 degrees. (B). AFM on dried sampled of fresh OS30 and OS90 worms reveals further information on the nature of the hinges. Regions of negative curvature are seen which could be the hinge points of the worm. The diameter of the OS30 and OS90 worms are found to be approximately 15 nm and 30 nm (+/- 5 nm) respectively.

where consistent, visually observable fluctuation (greater than 5 degrees) between neighboring

segments occurs. On an average, OS30 worms are found to have 3 hinges per 10 micron contour

length, whereas the higher molecular weight OS90 forms smoother and stiffer worms with less

than one hinge per 10 microns. In addition to hinges, the worms also contain immovable, rigid

bends, whose population is of the same order as that of the flexing hinges. To more accurately

quantify the backbone conformation of the OS30 worms, the distance between bends and the angle between bends was measured on the skeletonized backbones (**SI 1A**). The worm backbone was traced as a series of 0.5 micron segments, and considering the pixilation error, a deviation of over 30 degrees from the straight line between adjacent segments was considered a bend. The distance between bends is observed to have a peak at ~ 1-1.5 microns, while the angles have a slightly more uniform distribution with a slight peak around an obtuse angle of 110-120 degrees. It is likely that the OS30 worms have a persistence length of the order of ~1 micron when the chloroform evaporates and kinetically traps the backbone in the staggered geometry. The uniformity in the distribution of angles further supports this rapid shape-freezing hypothesis.

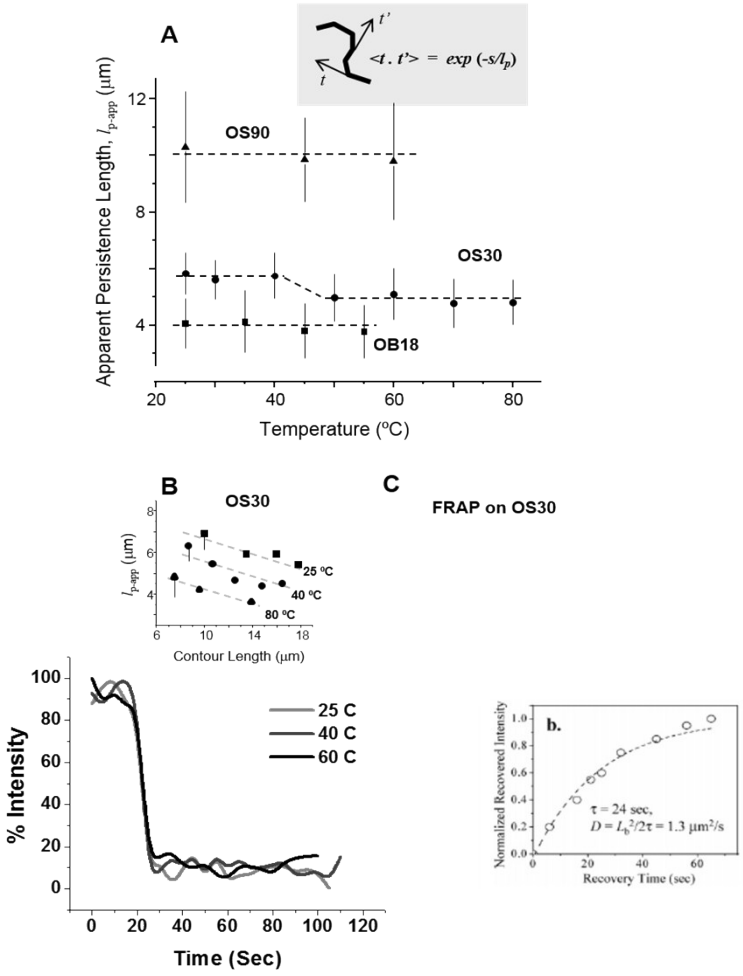

SI-2. Temperature effects. (A). The tangent-tangent correlation function was used to measure the effective persistence lengths of the glassy worms. (B). The tangent-tangent correlation method might not be the best way to estimate the flexibility of OS30 worms. The longer worms are consistently found to have a shorter persistence length for any temperature. (C). A focused laser beam was used to precisely bleach a small region (~ 1 mm radius) in the short OS30 worms.

Quantifying stiffness and temperature effects on rigidity The tangent-tangent correlation method was used to determine the persistence length of the stiff worms. The trace of the worm backbone was used to determine the angle between tangential unit vectors t, t' distances along the worm, and the effective persistence length l_p was calculated from the decay of the angle correlation according to the expression $\langle t \cdot t' \rangle = \exp(-s/l_p)$. Even though the worms have stiff, jagged features, they are long enough for the correlation average to decay fairly smoothly along the length of the worm. Thus this scheme might be a useful tool to quantify the rigidity of the worms, especially as a function of temperature. Thin films of lower molecular weight polystyrene are known to exhibit a suppression of glass transition temperature compared to the bulk value of 100 C. OS90 worms, which are around 30 nm in diameter do not exhibit any visible morphological change up to 60 C when observed under fluorescence microscopy. The tangent-tangent correlation length in this temperature range is measured to be constant at 10 +/- 1.8 μm (**SI 2A**). Lower molecular weight OS30 worms exhibit an increase in the rate and amplitude of oscillation about the hinges as the temperature is increased. However the tangent-tangent correlation length which shows only a weak transition around 45 °C, if any, does not capture this dynamical motion. The persistence length changes abruptly from 5.7 μm to 4.8 μm, which could indeed be a sign of a glass transition. Worm micelles of PEO-PBD (MW 11 KD) used as a control do not show any temperature dependence on the persistence length in this range of conditions. For OS30 worms, at any temperature, a consistent trend of shorter worms being stiffer is observed (**SI 2B**). This indicates the tangent-tangent correlation scheme may not be the best method to describe the rigid and hinged motion of the glassy worm. A better stiffness measurement scheme is needed, one that would also capture the fluctuation dynamics about the hinges as a function of temperature.

For a more local study of the glassiness as a function of temperature, FRAP over a small region of the worm was performed. A focused laser beam was used to completely photo-bleach a 2-4 μm length segment of the OS30 worms. There was no recovery observed in the bleached region for up to 2 minutes of continuous monitoring (**SI 2C**). At 60 ^{o}C, there is a very slight recovery observed after about 2 minutes. Though the marginal increase is observed in repeat experiments, it is still within the noise level and we are unable to make a firm conclusion regarding any breaking of glassiness. It is interesting to note that the transition in the persistence length of OS30 worms is also observed around the 50 ^{o}C mark. Previous light scattering and neutron scattering experiments on aqueous solutions of PS-PEO spherical micelles up to 95º C [12] have failed to notice any substantial change in the size or shape of the micelles. This further supports the idea that there might not be any real glass transition in the temperature range explored in our experiments. Slow relaxation dynamics are a characteristic feature of glassy systems, so a time course study of the structure of OS30 conformations was performed. No change in the distribution of hinges was observed up to 8 weeks. In some samples however, the kinks in the backbone appear to get smoothed out even before the 4-week mark, resulting in rigid, smooth worms, very similar to the OS90 worm morphology. The presence of trace quantities of residual solvent in the core is a likely cause for this occurrence. The effect of solvents on the worm morphology are explored in more detail in a separate section.

Shape change of the simulated worm in presence of model hydrophobic solvent

The variations of core radius, R_c, along the central axis of worm in presence of model organic solvent are shown in **SI 2A**. The average values ($<R_c>$) at different concentrations of hydrophobic solvent [C_s] are also presented in **SI 2B**. Data without any hydrophobic solvent is given for comparison. In agreement with density profile, core radius also increases with gradual increment

of solvent concentration, especially after 10 % solution. The larger radius of the PEO-PS assemblies is associated with the spherical morphology.

Next, to explore the PEO-PS interface with changing the shape of the worm micelle in presence of hydrophobic solvent, we calculate density fraction (ρ_f) of both PEO and PS as a function of distance from the central core region. ρ_f of PEO and PS are defined as $\frac{\rho_{PEO}}{\rho_{PS}+\rho_{PEO}}$ or $\frac{\rho_{PS}}{\rho_{PS}+\rho_{PEO}}$ respectively. In the core and the corona regions, the density fractions are always 1 for PS and PEO respectively. But, at the interface both PEO and PS coexist simultaneously. Hence, we can easily identified the PEO-PS interface from the variation of ρ_f as function of distance from the core. Results are shown in **SI 3C.** Average width (D_w) of the interface in presence of hydrophobic solvent at different concentration are also given in **SI 3D.** It is evident from the figure that as the worm like micelle transfer to spherical micelle with increasing solvent concentration, the width of the PEO-PS interface also increases simultaneously.

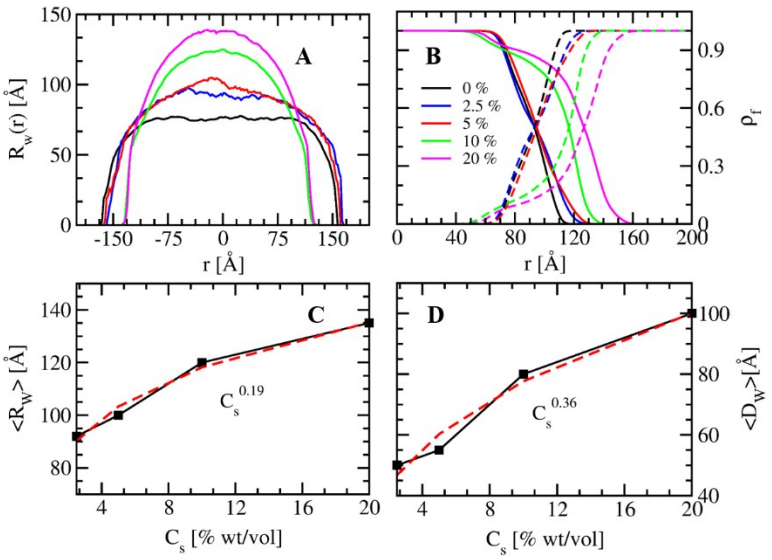

SI-3 (A) Variations of core radius (R_w) and (B) density fraction (ρ_f) along the central axis of worm in presence of model organic solvent. The average (C) core radius (<R_w>) and (D) width of the PEO-PS interface (D_w) as a function of hydrophobic solvent concentration. Solid and dotted line in figure SI-6 B are the density fraction for PS and PEO respectively.

Variation of Maximum PEO and PS Density with Increased Solvent

We also **c**haracterize the maximum PEO and PS density in the corona and brush respectively. We find that the maximum PS density exhibits a scaling with respect to the concentration of salt,

$\rho_{max} \sim C_s^{-.126}$. The maximum PEO density does not substantially vary as a function of increased solvent concentration.

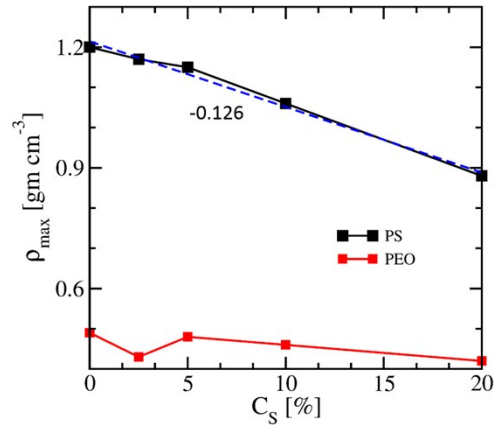

SI-4 Variation of the maximum density of PEO and PS in presence of hydrophobic solvent.

Quantifying Shape Change in Simulation

In the experiments, three different solvents (chloroform, xylene and toluene) with different polarity were chosen in order to study the solvent effect. Compared to toluene or xylene (more hydrophobic), the worm-like morphology of OS30 remains stable in a more concentrated chloroform (less hydrophobic). Like the experiment, we performed two additional simulations of OS30 in presence of 10 % solution with increasing polarity of the solvent and compared the shape change by characterizing the shape of the micelle. Specifically, we calculate the ratio of the maximum to minimum moments of inertia of the micelle = $R_r = I_{max} / I_{min}$ where $I_{micelle} = \sum_{i \in micelle} m_i r_i^2$. See **SI 5.** Increase in R_r, with increasing solvent polarity clearly reveals that worm morphology remains more stable in presence of a less hydrophobic solvent and it agrees well the experiment. To vary hydrophobicity (polarity as shown in graph), we change the Lennard Jones parameter ε of the model solvent with itself from 0.312 to 0.4491 to

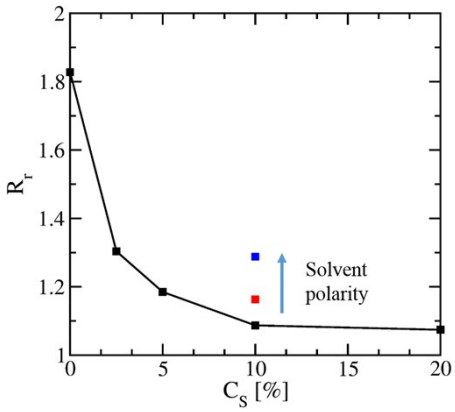

SI-5 Variation of the average ratio of longest and shortest principle axis of worm in presence of hydrophobic solvent. With increasing solvent polarity shape of micelle remains more worm like.

0.895. We also increase the interaction with all other coarse grain beads using the mixing rule. We perform 50 ns simulations under NPT conditions.

Distribution of hydrophobic solvents within the worm Distribution of hydrophobic solvents within the worm core at four different concentrations are shown in **SI 6**. Depending on distributions of the hydrophobic solvent inside the worm core, two different types of structures of the aggregate is clearly visible from the figure. At lower concentration, the structure is more analogues to simple solubilization model. With increasing solvent concentration, the structure of the aggregate changes to droplet microemulsion with a pure solvent pool in the center of the core. The solvent pool also increases with increasing solvent concentration.

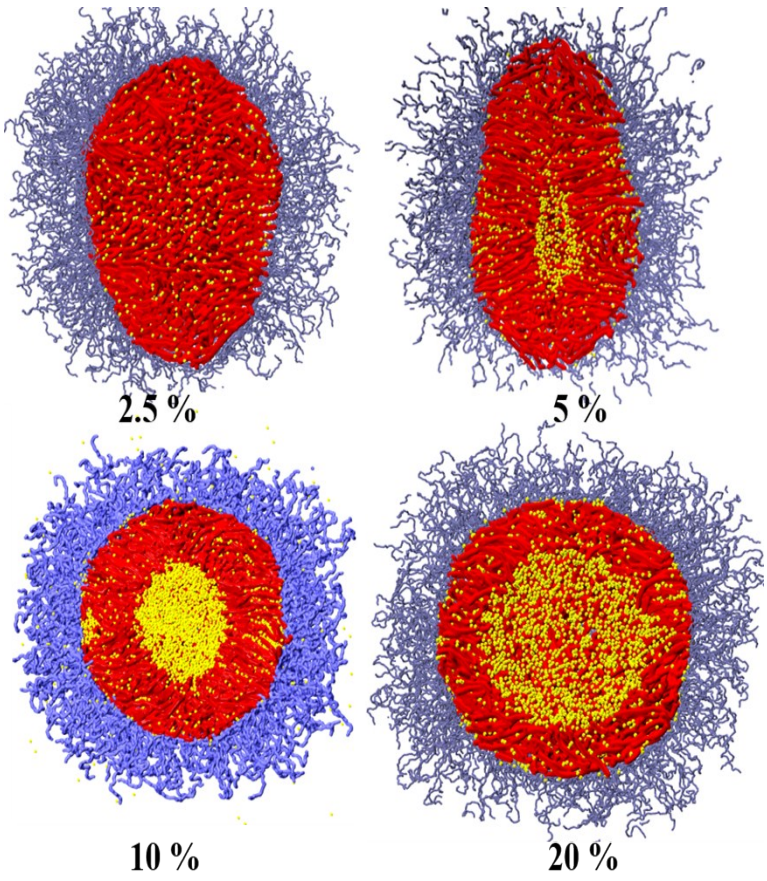

SI-6 Distribution of hydrophobic solvent within the worm at different concentrations. Here solvent is shown in yellow color and PEO and PS in blue and red color respectively.

1. G. Fiorin, M. L. Klein, R. DeVane and W. Shinoda, in *Hierarchical Macromolecular Structures: 60 Years after the Staudinger Nobel Prize II*, Springer International Publishing, 2013, pp. 93-107.
2. W. Shinoda, R. DeVane and M. L. Klein, *Current Opinion in Structural Biology*, 2012, **22**, 175-186.
3. S. C. L. Kamerlin, S. Vicatos, A. Dryga and A. Warshel, *Annual Review of Physical Chemistry*, 2011, **62**, 41-64.
4. S. M. Loverde, M. L. Klein and D. E. Discher, *Advanced materials*, 2012, **24**, 3823-3830.
5. W. Shinoda, D. E. Discher, M. L. Klein and S. M. Loverde, *Soft Matter*, 2013, **9**, 11549-11556.
6. S. M. Loverde, V. Ortiz, R. D. Kamien, M. L. Klein and D. E. Discher, *Soft Matter*, 2010, **6**, 1419-1425.
7. M. Drenscko and S. M. Loverde, *Molecular Simulation*, 2017, **43**, 234-241.
8. W. Shinoda, R. DeVane and M. L. Klein, *Molecular Simulation*, 2007, **33**, 27-36.
9. W. Shinoda, R. DeVane and M. L. Klein, *Soft Matter*, 2008, **4**, 2454-2462.
10. X. He, W. Shinoda, R. DeVane and M. L. Klein, *Molecular Physics*, 2010, **108**, 2007-2020.
11. V. Percec, D. A. Wilson, P. Leowanawat, C. J. Wilson, A. D. Hughes, M. S. Kaucher, D. A. Hammer, D. H. Levine, A. J. Kim, F. S. Bates, K. P. Davis, T. P. Lodge, M. L. Klein, R. H. DeVane, E. Aqad, B. M. Rosen, A. O. Argintaru, M. J. Sienkowska, K. Rissanen, S. Nummelin and J. Ropponen, *Science*, 2010, **328**, 1009-1014.
12. K. Mortensen, W. Brown, K. Almdal, E. Alami and A. Jada, *Langmuir*, 1997, **13**, 3635-3645.